Real-time measurements of temperature, pressure and moisture profiles in High-Performance Concrete exposed to high temperatures during neutron radiography imaging

N. Toropovs [a,b,*], F. Lo Monte [c], M. Wyrzykowski [a,d], B. Weber [a], G. Sahmenko [b], P. Vontobel [e], R. Felicetti [c], P. Lura [a,f]

[a] *Empa, Swiss Federal Laboratories for Materials Science and Technology, Dübendorf, Switzerland*
[b] *Riga Technical University, Institute of Materials and Structures, Riga, Latvia*
[c] *Politecnico di Milano, Department of Civil and Environmental Engineering, Milan, Italy*
[d] *Lodz University of Technology, Department of Building Physics and Building Materials, Lodz, Poland*
[e] *Paul Scherrer Institute, Laboratory for Neutron Scattering and Imaging, Villigen, Switzerland*
[f] *ETH Zürich, Institute for Building Materials (IfB), Zürich, Switzerland*

Received 16 July 2014
Accepted 8 November 2014 Available online 8 December 2014

1. Introduction

1.1. Spalling theories and preventive measures

High-Performance Concrete (HPC) is a modern building material with superior properties compared to traditional concrete [1]. HPC is characterized by high compressive and tensile strengths, high modulus of elasticity, low permeability, high resistance to abrasion and good du-rability. By reducing the construction dead weight, fewer raw materials are consumed and slender and elegant constructions with lower embodied energy become possible. HPC is used in high-rise buildings, long span bridges, thin walled (especially prefabricated and pre-stressed) elements for building façades, prefabricated columns, ele-ments for tunnels, etc.

A major limitation to the widespread use of HPC comes from its sen-sitivity to explosive spalling when exposed to fire [2,3]. Spalling reduces the concrete cover of reinforcement and may lead to premature failure of reinforced concrete members. The first theories about spalling mechanisms go back to the 1960's ([4,5], see also [6]). According to the *pressure build-up theory* [4], water accumulates behind the drying front because vapor produced at the drying front migrates towards the colder inner region, where it condenses. The condensed vapor re-duces the gas permeability and may cause liquid water saturation of the pores, referred to as the *moisture clog* [2,7]. At the same time, the high rate of vaporization on the hot side of the moisture clog, together with the thermal dilation of vapor and air due to heating, induces gas pressure build-up in the pores. This process may lead to spalling if the solid pressure acting on the concrete stiff skeleton due to the gas pressure exceeds the tensile strength of the concrete (which at high temper-atures is reduced by cracking and dehydration) [8].

Another possible mechanism of spalling is described by the *thermal stresses theory* [5]. Since the temperature at the moisture clog is close to 100 °C and the surface temperature increases rapidly while the depth of the dry layer is still small, a steep thermal gradient develops between the heated surface and the moisture clog, which induces high thermal stresses. According to Saito [5], spalling is due to compression failure near the heated surface. Based on a detailed analysis of pore pressure and thermal stresses, Sertmehmetoglu [4] proposed that the compressive stresses near the heated surface result in tensile cracks parallel to the surface. The gas pressure developing in these cracks, moreover,

* Corresponding author at: Riga Technical University, Institute of Materials and Structures, Riga, Latvia. Tel.: +371 27062210.
E-mail address: nikolajs.toropovs@rtu.lv (N. Toropovs).

induces explosive spalling. Failure is further eased by stress concentration at the crack tips and by buckling due to compression.

It needs to be underlined that the mechanisms proposed by the two theories (pressure build-up and thermal stress) are strongly coupled and both dependent upon the moisture distribution (and upon the formation of the moisture clog) during fire.

A number of key parameters influencing spalling have been singled out and extensively studied [6,9,10]. However, despite the large body of research, predicting the occurrence of spalling has proven to be an elusive task and current explanations of spalling behavior are mostly empirical and qualitative. It is commonly accepted, however, that high moisture content favors the formation of the moisture clog, slowing down the drying front and increasing the temperature gradient [6]. High heating rate also increases the gradient, while external loads or confinement contribute to increase of the stress [6].

Focusing in particular on the moisture clog, the risk of fire spalling increases when the internal relative humidity (RH) and the water satu-ration of pores are high, since a higher amount of moisture in the pores may lead to faster clogging. On the other hand, maintaining high RH in HPC is beneficial for reducing self-desiccation shrinkage and early-age cracks. Due to its low water-to-binder ratio (w/b), HPC can experience a considerable decrease of internal RH when the pores are partially emptied of water by the hydration process [11]. As a result, excessive self-desiccation shrinkage may lead both to macroscopic cracking in concrete members and to microcracking within the cementitious ma-trix. An efficient method for reducing self-desiccation shrinkage and at the same time promoting cement hydration is internal curing by means of superabsorbent polymers (SAP) [12]. The method is based on adding to the mixture dry SAP, that absorb water upon mixing and form small (100–200 μm across) water reservoirs uniformly distributed in the matrix [12]. When the hydration process binds mixing water and empties the capillary pores, water migrates from these water reservoirs and allows maintaining a high internal RH in the concrete, thereby reducing or eliminating self-desiccation shrinkage [12].

An effective method to reduce concrete spalling sensitivity is to add polypropylene fibers (PP-fibers), e.g., [9,13,14], which favor the pore pressure release and limit the formation of the moisture clog [14], thanks to an increase of concrete permeability caused by their melting at about 160–170 °C. PP-fibers have, however, several drawbacks (cost, reduced workability) and the exact mechanisms by which they reduce the probability of fire spalling have not yet been fully understood [14–17]. The combination of PP-fibers and SAP has been recently shown to be beneficial in reducing the risk of fire spalling [18], likely thanks to better connectivity among the fibers enabled by SAP voids, thereby pro-viding better protection against spalling at lower fiber content [18].

Because of the two contradictory premises, namely the higher inter-nal RH needed for reducing shrinkage and cracking, and, on the other hand, the increased risk of fire spalling, studying HPC with SAP addition and relatively high moisture content during heating is of practical rele-vance and has been the main motivation for this study. Furthermore, the main goal of the present paper is to propose and illustrate with some examples an experimental procedure designed for casting light on the mechanisms behind spalling and provide valuable input for both nu-merical approaches and mixture design.

1.2. Study of mechanisms underlying spalling

To understand the complex mechanisms underlying fire spalling, it is paramount to follow the moisture distribution in concrete during exposure to high temperature, quantitatively and non-destructively, in real time [19]. An effective method to measure water distribution in concrete is neutron radiography [20]. In concrete, aggregates and anhydrous cement weakly interact with neutrons, while hydration products and water-filled capillary pores have the largest interaction (mainly neutron scattering), leading to strong attenuation of an incident neutron beam. The application of neutron radiography to study water transport in cementitious materials subjected to high temperatures was already suggested in [21]; this idea, however, has been followed only recently [22,23]. Weber et al. [22] performed neutron radiography on small mortar slabs (dimensions $80 \times 80 \times 10$ mm^3) standing on a heating element and heated up to 600 °C in 15 min. In order to obtain 1-D temperature and moisture fields, the specimens were insulated against moisture and heat loss using aluminum foil and glass foam, except from the bottom and top edges. Temperature profiles were measured via embedded thermocouples and quantitative moisture profiles were obtained by means of neutron radiography [22].

As concerns pore pressure, several authors have directly performed measurements in concrete specimens subjected to thermal transients (see for instance [2,3,13,24]). This was generally performed by embed-ding thin stainless steel pipes provided with external electronic sensors. Possible alternatives [25] come from the adoption of a porous sensing head (to measure the mean pressure of larger paste volumes) and filling the pipe with thermally stable silicon oil (to prevent moisture leakage and minimize the compressible gas volume). Pressure sensors were cast at different distances from the heated surface of concrete and the pressure was measured together with the temperature [24,25]. Consistent results were generally obtained in different test conditions (concrete grade, moisture content, heating rate) and values as high as 4–5 MPa were reported in the case of HPC [25], while lower values were reported for normal-strength concrete [3]. For a better under-standing of spalling mechanisms, the results of pore pressure measure-ments should be directly compared with the moisture profiles inside the sample during thermal loading, which might in particular reveal the formation of moisture clogs. First attempts in this direction have been recently made by combining proton-spin relaxation NMR and pressure sensors [26].

In this study, neutron radiography was applied to investigate the water distribution in mortar samples heated from one side up to 550 °C. The samples were mortar slabs with dimensions of $25 \times 100 \times 100$ mm^3 standing on a heating plate, with the 100×100 mm^2 face exposed to the neutron beam (Fig. 1b). In addition, the temperature distribution within the samples was obtained by means of a series of thermocouples and the vapor pressure at two different locations was measured via pressure sensors [27]. This paper presents this new type of combined measurements and shows some preliminary results. In total, 16 tests were performed on mortar samples at different ages and with different compositions. The results presented in this paper regard two types of high performance mortar. The first sample was a mortar with SAP, which is expected to be prone to explosive spalling due to high moisture content (see [12,28]), while the second sample was a mortar with a combination of SAP and PP-fibers, where the risk of spalling should be reduced [18].

2. Materials and test set-up

2.1. Mixing and sample preparation

The cross-section of the samples was chosen to fit into the field of view of the neutron beam, which was 150×150 mm^2. Thin samples are preferred because they do not induce too large neutron attenuation, thus avoiding the need of long exposure time of the camera to achieve a satisfactory signal-to-noise ratio, and limit artifacts due to sample scattering. At the same time, the samples needed to be thick enough com-pared to aggregate size, especially to accommodate the pressure sensor heads, which were embedded in the samples during casting. Moreover, thick samples should allow minimizing the boundary effects on the moisture profile along the plate thickness (direction perpendicular to the observed plane). Based on these constraints, mortar samples with dimensions of $100 \times 100 \times 25$ mm^3 were cast.

High-performance mortars with w/b equal to 0.34 were mixed using a 5-l Hobart mixer (the mix composition is presented in Table 1). The binder was Portland cement CEM I 52.5R blended with undensified

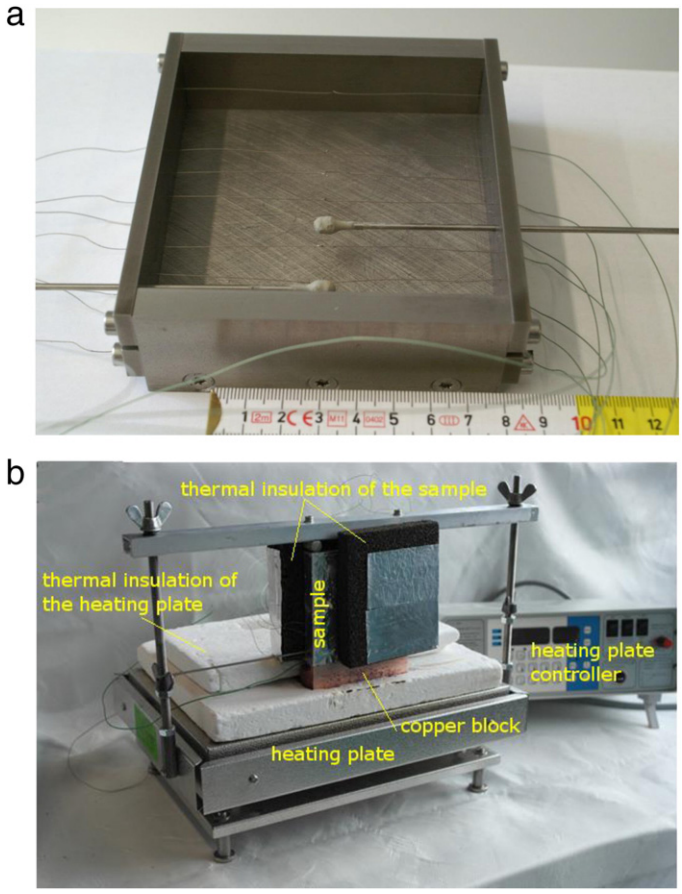

Fig. 1. a) Mold fitted with thermocouples and two pressure sensors; b) arrangement of the sample during the test. The sample is moisture-sealed using high-temperature resistant adhesive aluminum foil and thermally insulated by means of black glass foam (partially stripped for the demonstration). The sample is placed on a copper block that allows conducting the heat from the heating plate (the remaining surface of the plate is covered by white ceramic insulation plates). Note that during neutron radiography manometers were fixed at the ends of the capillary tubes and the sample was placed inside a thin aluminum box to protect the neutron detector from spalling debris.

silica fume at a mass proportion of 4:1. Here, the results for two mortars are presented: with addition of SAP (denoted as SAP) and with addition of SAP and PP-fibers (denoted as PP + SAP)

Dry solution-polymerized SAP of sizes 63–125 μm were added to the mixture in the amount of 0.33% by weight of binder. The SAP saturate with pore fluid and form water reservoirs in the fresh mortar. After in-ternal curing has taken place in the initial days of hydration [29,30], voids of 100–200 μm size, partially filled with hydration products (mainly calcium hydroxide), remain in the mortar [31].

In the PP + SAP mortar, PP fibers of 3 mm length and 30 μm diameter were added in the amount of 0.34% by mass of binder (corresponding to 2 kg per m^3 of mortar). Polycarboxylate ether-based superplasticizer was used to improve the workability of the mixtures. The mortars contained 60% by volume of alluvial sand (sandstone, limestone, dolomites and metamorphic rocks) with grains up to 4 mm.

Table 1
Mix composition [kg/m^3].

Mortar type:	SAP	PP + SAP
Cement CEM I 52.5 R	464	464
Silica fume	116	116
Aggregate 0–4 mm	1582	1582
Superplasticizer	8.12	14.5
PP fibers	0	2
SAP	1.93	1.93
Water	197.2	197.2
W/b total	0.34	0.34

Firstly, thermocouples and capillary tubes were fitted to the molds (Fig. 1a) and then the mortar was carefully cast into the mold, placed on a vibration table. The samples were next covered with plastic sheets and placed at 20 ± 0.3 °C and >95% RH. After demolding at 1 day, the samples were sealed in plastic bags and stored at 20 ± 0.3 °C and 95 ± 3% RH until the age of about 3 weeks (18 days and 22 days for PP + SAP and SAP sample, respectively), when the tests were carried out. Seven thermocouples (type K, Ø = 0.2 mm, all welded) were em-bedded directly into the samples during casting (Fig. 1a). The nominal position of the thermocouples was 5, 15, 25, 45, 55, 65, and 95 mm from the heated side. The actual position of the thermocouples was de-termined by performing X-ray radiography on the samples immediately before the test (Fig. 3a).

The pore pressure measurements were performed by means of capillary steel pipes (Ø = 2 mm) with heads made of sintered metal fitted on their ends (Ø = 5 mm) (Fig. 1a). Before casting, the heads were dipped in dense cement paste in order to avoid penetration of fluid cement paste during casting. The nominal position of the sensors was 10 and 35 mm from the heated side. Immediately before the tests, the pipes were filled with silicone oil and one additional thermocouple was inserted into each pipe.

2.2. Heating of samples

The arrangement of the sample on the heating block is presented in Fig. 1b. Before heating, the samples were insulated against moisture and heat loss. Aluminum foil (almost transparent to neutrons) provided with high-temperature silicone adhesive was applied on all faces except the bottom (heated) face to avoid vapor loss. The aluminum foil

prevents the sample from drying out, but it does not provide a tight sealing that would allow for a large pressure build-up. The sides of the sample were then thermally insulated using a 20 mm-thick glass foam layer which was finally wrapped with aluminum tape to hold it in posi-tion. The manometers were then mounted onto the ends of the capillary tubes and the sample was placed on the heating device (a programma-ble heating plate). During neutron radiography, the sample had to be positioned close to the scintillator, while the heating plate needed to be kept away from the field of view. Furthermore, the goal was to heat only the bottom of the sample and to limit the heating of the sides by convection. In order to meet these constraints, a copper element was in-terposed as heat conductor between the sample and the heating plate. This element had its bottom face laid directly on the heating plate, and the dimensions of the top face fitted just to accommodate the sample. This arrangement allowed placing the ceramic insulation plates all around the copper conductor and minimizing the heating of the sample sides and of the surrounding neutron imaging facilities. The temperature of the copper block below the sample was measured by means of a thermocouple. The sample was then fixed on the heating plate/copper block with an aluminum frame pressing on its top edge (see also Fig. 3b). Finally, in order to protect the surroundings (especially the detector) from spalling debris, the sample was contained within an aluminum box with a 1 mm-thick wall. The heating plate was programmed to reach 550 °C in 12 min and hold the temperature for the following 2 h.

2.3. Neutron and X-ray radiographies

Neutron radiography was performed at the NEUtron Transmission RAdiography (NEUTRA) beamline of the Paul Scherrer Institute (PSI) in Villigen, Switzerland. This beamline is fed by the Swiss Neutron Spallation Source (SINQ) and is operated with neutrons within a thermal spectrum characterized by a Maxwell-like probability density function, with a most probable energy level of about 25 meV [20]. The detector setup used consists of a 100 μm thick ^{6}Li doped ZnS screen imaged by a fast readout sCMOS system (Andor Neo). The sample face was fixed at a distance of 55 ± 1 mm from the scintillator. The field of view had a size of 124 × 147 mm^2 with a nominal pixel size of 57.5 × 57.5 μm^2. The exposure time for a single image was 14 s and the total image acquisition time was about 18 s, providing an image frame rate of about 3.5 frames per minute.

The intensities measured in the neutron radiography are related to absorption and scattering of neutrons by the sample. The attenuation of the intensity I follows the exponential law of radiation attenuation (Beer–Lambert law):

$$I(x,y) = I_0(x,y)e^{-\int \Sigma(x,y,z)\,dz} \tag{1}$$

where I_0 is the intensity of the incident neutron beam and Σ is the effective attenuation cross-section, which depends on the sample material.

We assume that the material basically consists of water in free or chemically bound form and of dry components (anhydrous cement, aggregates), each characterized by an equivalent thickness. We further assume that the change of attenuation due to vaporization of hydrogen from SAP and PP-fibers should be negligible, based on the very low concentration of the polymers in the mortars compared to their water content. The attenuation can then be written as

$$I(x,y) = I_0(x,y)e^{-\Sigma_w d_w(x,y)-\Sigma_c d_c(x,y)} \tag{2}$$

where Σ_w and Σ_c are the effective attenuation cross-sections of water and of dry components (binder, aggregates, polymers, etc.), respectively, and d_w and d_c are the corresponding equivalent thicknesses.

The neutron beam transmission coefficient T is then

$$T(x,y) = \frac{I(x,y)}{I_0(x,y)} = e^{-\Sigma_w d_w(x,y)-\Sigma_c d_c(x,y)} \tag{3}$$

Assuming that only the water content changes during the experiment, the variation of the equivalent water thickness $\Delta d_w = d_w(x,y,t) - d_w(x,y,t_0)$ is determined as:

$$\Delta d_w(x,y,t) = -\frac{1}{\Sigma_w}\ln\frac{T(x,y,t)}{T(x,y,t_0)} \tag{4}$$

Before calculating the equivalent water thickness, the recorded images have to be corrected for camera electronic noise (dark current correction), backscattering of neutrons (black body correction), and spatial and temporal inhomogeneities of the neutron beam or of the scintillator screen (flat field correction), see [32,33].

Other effects such as sample scattering and beam hardening have been accounted for by calibrating the whole measuring setup with the effective attenuation cross-sections of water. To this end, an aluminum container with twelve water steps (thickness from 1 to 12 mm) placed in the neutron beam direction has been analyzed (see also [32]). By using Eq. (4) with the empty container as the initial state and the filled container as the final state, the curve labeled "uncorrected" in Fig. 2a was obtained, assuming a constant cross-section for water equal to $\Sigma_w = 0.35$ mm^{-1}.

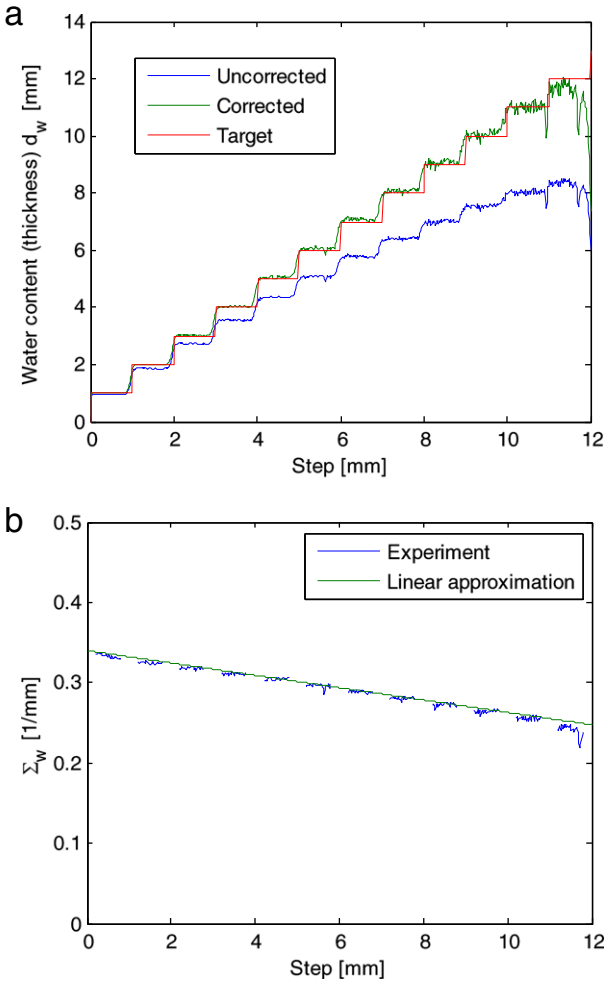

Fig. 2. Variable macroscopic cross-section accounting for sample scattering and beam hardening: a) corrected and uncorrected water contents in the water steps; b) calculated cross-section of water. The equivalent thickness of water in the mortar samples at the start of testing is equal to 5 mm.

For the correction, the cross-section has been calculated using Eq. (4) and taking for Δd_w the geometric water thickness. As shown in Fig. 2b, the cross-section changes linearly with the water thickness. By using this variable cross-section, the corrected curve for the water steps can be constructed as shown in Fig. 2b. Note that the original, i.e. assuming no water loss from the sample, water thickness calculated from mix design, where roughly 20% of sample volume is occupied by water (see Table 1), is 5 mm in the mortar samples considered here. Alternatively, a simulation of the sample scattering has been proposed for the scattering correction [32]. However, based on the simple 2-D geometry of our experiments, and considering also the complex simula-tion procedure [32], a simple scheme based on measurements on water steps was considered sufficient for correcting the sample scattering and beam hardening artifacts.

Before heating tests and neutron imaging took place, X-ray radiographies of all samples were acquired in order to determine precisely the positions of thermocouples and pressure sensors. This was possible thanks to the additional X-ray tube and detector available at the NEUTRA imaging facility. A voltage of 100 kV was applied to accelerate the electrons and the current of the electron beam was 15 mA.

3. Results and discussion

Fig. 3a shows an X-ray radiograph of the sample that was acquired in order to determine the exact position of the thermocouples and of the pressure sensor heads. Fig. 3b shows an exemplary neutron radiography image in which the drying front in the PP + SAP sample after 24 min of heating is evident. Some boundary effects are visible near the vertical edges of the sample, due to imperfect sealing that led to faster drying. In order to exclude these boundary effects in the evaluation of the mois-ture profiles (see Fig. 6), only the region indicated by the rectangular frame in Fig. 3b was considered for averaging the moisture content changes.

As could be expected based on the findings presented in [18], the ad-dition of both SAP and PP-fibers allowed avoiding spalling. On the other hand, spalling occurred after 24 min of heating in the sample with SAP only (Fig. 4). Spalling took the form of a large crack parallel to the heated surface along the whole length of the slab at a height of about 6 mm (corresponding to the position of the drying front, see Figs. 4 and 6b).

The temperature profile was determined by fitting spline curves (Fig. 5) to the readings of the embedded thermocouples, whose locations were determined via X-ray radiography (Fig. 3a). Note that the temperature at the height of 0 mm was assumed equal to the tempera-ture of the copper block on which the sample was placed. Only the lower 35 mm near the heated surface is shown. There is no marked difference between the temperature profiles in the two samples, albeit the spatial resolution of the thermocouples is not fine enough for a precise assessment.

The water loss profiles (expressed as equivalent water thickness [34]) are shown in Fig. 6. The mixing water occupied approximately 20% of the mortar volume (see Table 1), which for a sample thickness of 25 mm corresponds to an initial equivalent water thickness of 5 mm. The water being the difference between the moisture content at time t and at t_0 (start of heating) was calculated with Eq. (4). The profiles were obtained by averaging at each height the change in moisture content along the horizontal line enclosed by the region indicated in Fig. 3b. The profiles feature a plateau corresponding to a sudden change in slope where the water loss changes rapidly from almost zero to a large negative value over a small height. The approximate position (height) of the plateau therefore indicates the drying front, where a large portion of free and chemically bound water disappears by vapor-ization and dehydration, respectively. Since the drying takes place in a certain narrow region, the plateau is not perfectly horizontal but ex-tends over a certain height.

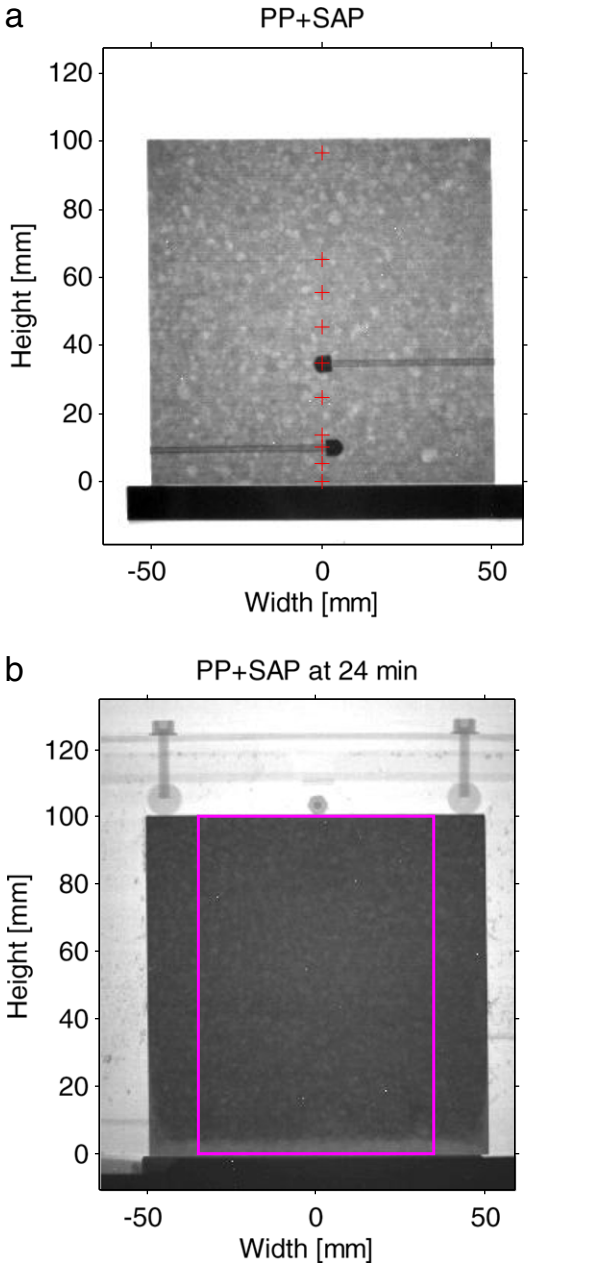

Fig. 3. a) X-ray raw radiography image showing the position of the thin thermocouples (indicated with crosses) and of the pressure sensor heads, b) neutron raw radiography image after 24 min of heating. The drying front is clearly visible. The rectangular contour in Fig. 3b indicates the averaging region for obtaining the moisture profile (Fig. 6). The gray levels refer to beam intensity.

No moisture accumulation behind the drying front is evident in Fig. 6, in contrast to the first pilot tests [22]. The drying front moved faster in the sample with PP + SAP compared to the sample with SAP only and did not show any sharp change in slope. This is likely due to the increase of permeability occurring when PP-fibers melt and form channels through which the vapor can be evacuated [35,36]. On the other hand, a sharp change in the water loss is visible in the SAP sample in correspondence with the position of spalling, Fig. 6b. Knowing that dehydration consumes energy, the moisture profiles allow inferring that the temperature profiles are also smoother and thermal stresses should be reduced when PP-fibers are added. The moisture profiles can therefore complement the temperature measurements that were not obtained with sufficient spatial resolution in this experiment.

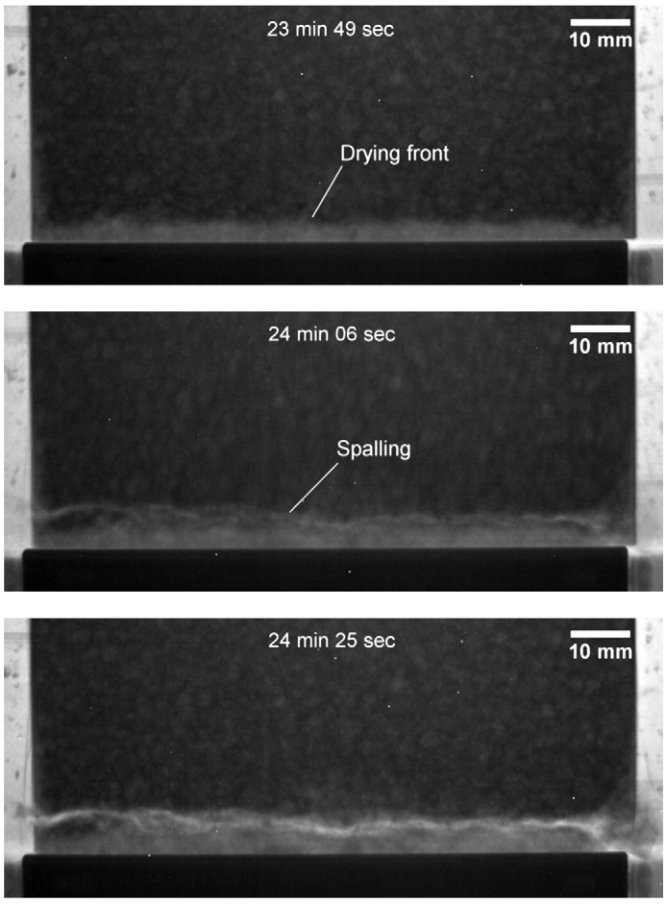

Fig. 4. Sequence of raw neutron radiographs (cropped bottom part of the sample) showing drying and spalling in the SAP mortar. Time 23:49: just before spalling, the dried region is visible in brighter gray values. Time 24:06: the spalling crack appears first as a fine line and widens in the successive radiographs. The gray levels refer to beam intensity.

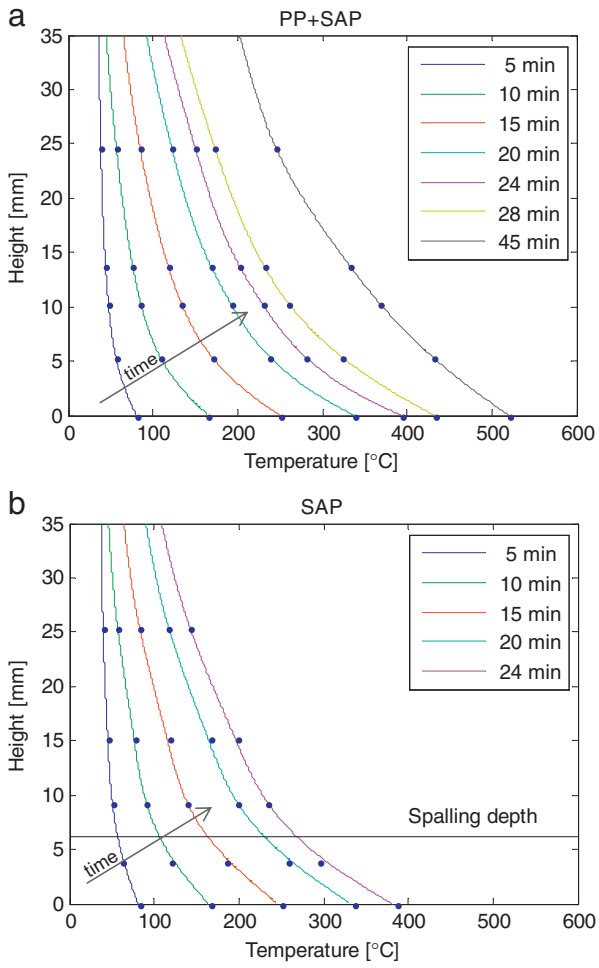

Fig. 5. Temperature profiles of lower 35 mm of the mortar slab: a) PP + SAP sample (no spalling), and b) SAP sample (spalling occurred after 24 min at 6 mm height).

The pore pressure measured by the pressure sensors (placed at 10 and 35 mm from the heated face) is shown in Fig. 7 as a function of time. The pressure peak is expected to be correlated to the drying front, where water loss proceeds at the highest rate. This is confirmed by the water loss profiles in the PP + SAP sample. It can be seen in Fig. 6a that the drying front (understood as the region where the moisture change profile shows a plateau) reaches the position of the first pressure sensor (located at 10 mm from the heated side) at about the same time when the maximum value of pressure is measured (compare the change of slope of the 28-min profile at approximately 10 mm height in Fig. 6a with the occurrence of the pressure peak at that time at the 10 mm position in Fig. 7a).

The pressure in the sample with no PP-fibers (Fig. 7a) is shown only up to the spalling event, since afterwards it is greatly influenced by the pressure release through the spalling crack. But even up to the spalling event, the pressure increases less than in the sample with PP-fibers (Fig. 7a). This is consistent with the slower evolution of the drying front in the sample with no PP-fibers (Fig. 6b), which suggests a slower advancement of the pressure peak and thus a larger distance from the pressure sensor at a given time (similar results were found by Kalifa et al. [13]). Before the pressure peak could reach the first sensor, spalling took place at a lower position in the SAP sample. Once spalling occurred, the pressure could suddenly be released through the spalling crack and the heat transfer between the copper block and the sample became less effective.

Fig. 7 shows also the vapor saturation pressure curve as a function of time, at the location of each pressure sensor. Unlike in [2,3], the pressure does not appear to follow the equilibrium vapor pressure.

4. Conclusions

Neutron radiography has been performed on mortar slabs exposed to heating up to 550 °C, simultaneously monitoring temperature and pore pressure. In this paper, the results obtained on two mortars with the same water-to-binder ratio equal to 0.34 are presented, the former with PP-fibers and SAP and the latter with SAP only. Since the addition of SAP leads to high moisture contents, the risk of spalling is expected to increase with respect to HPC without internal curing. Spalling occurred in the mortar with SAP only in correspondence of the drying front at a temperature of approximately 260 °C. On the contrary, no spalling took place in the PP + SAP mortar. Thanks to the combined measurements of temperature, pore pressure and moisture distribution, the behavior of the mortars during heating has been investigated comprehensively. This approach is expected to provide new insight in the study of fire spalling mechanisms.

No considerable difference could be observed regarding temperature profiles between the two samples (with and without PP-fibers). The positioning of thermocouples, however, allows for only limited resolution of the temperature profiles; nevertheless, this gap can be bridged by the simultaneous measurement of the moisture profile by means of neutron radiography. Smoother moisture profiles could be observed for the mortar with PP-fibers, suggesting in this case also a less steep variation of the temperature. This could significantly reduce thermal stress and pressure concentrations, and thus the spalling risk. The smoother moisture profile and the faster movement of the drying front are most likely due to increased permeability occurring thanks to

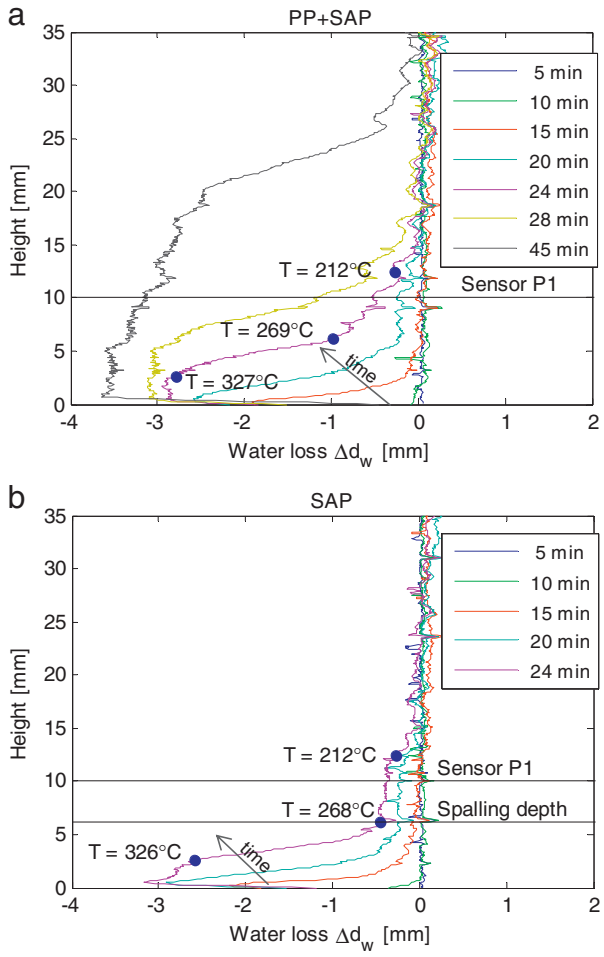

Fig. 6. Water loss profiles (expressed as equivalent thickness) of the lower 35 mm of the mortar slab (note that the profiles were measured for the whole height of the sample): a) PP + SAP sample (no spalling); b) SAP sample (spalling occurred after 24 min at 6 mm height). Estimated temperatures at 24 min are indicated for characteristic points of the profile.

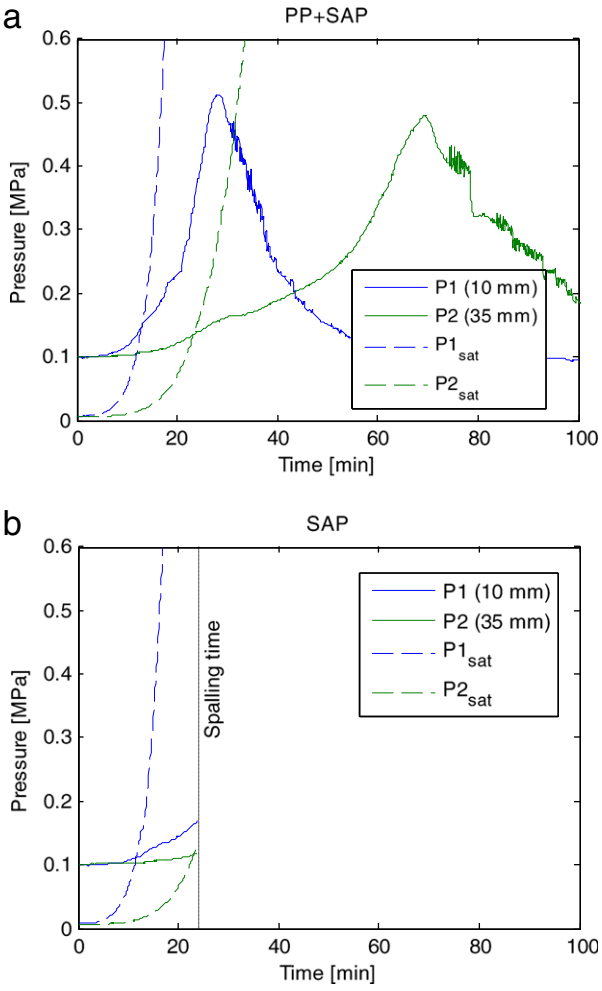

Fig. 7. Pore pressure measured by the two sensors P1 and P2 (nominal distance from the heated side indicated): a) PP + SAP sample (no spalling); b) SAP sample (spalling occurred after 24 min at 6 mm height). Vapor saturation pressure curves (calculated on the basis of the temperature measured in correspondence of the sensors) are also reported.

PP-fibers melting. In the sample with SAP only, the moisture profiles experience a sharp change in slope, indicating a clear drying front, in correspondence of which spalling occurred.

The comparison between the moisture profiles and the pressure development allows inferring that the peak pressure occurs within the drying front. Thus, the more localized and more slowly advancing drying front observed in the sample without PP-fibers supports also a narrower pressure peak, which develops closer to the heated face.

Acknowledgments

This study was partially funded by the Scientific Exchange Programme Sciex NMS-CH under the project 12.305 “FRESCO-Fire spalling of High Performance and Ultra-High Performance Concrete”. We would like to thank Dr. Pierre Pimienta from CSTB for his valuable discussion on the mechanisms of spalling and on experimental techniques. We also thank Dr. Michele Griffa (Empa) for critical reading of the manuscript and Mr. Carmelo Di Bella (Empa) for his help during samples preparation. The measurements were performed at the NEUTRA beamline at PSI. The help of Dr. Eberhard Lehmann and Mr. Jan Hovind from the Neutron Imaging and Activation Group (NIAG) at PSI is gratefully acknowledged.

References

[1] A. Neville, P.-C. Aïtcin, High performance concrete—an overview, Mater. Struct. 31 (1998) 111–117.
[2] P. Kalifa, F.-D. Menneteau, D. Quenard, Spalling and pore pressure in HPC at high temperatures, Cem. Concr. Res. 30 (2000) 1915–1927.
[3] J.-C. Mindeguia, P. Pimienta, A. Noumowé, M. Kanema, Temperature, pore pressure and mass variation of concrete subjected to high temperature — experimental and numerical discussion on spalling risk, Cem. Concr. Res. 40 (2010) 477–487.
[4] G. Shorter, T. Harmathy, Discussion on the fire resistance of prestressed concrete beams, Proc. Inst. Civ. Eng. 20 (1961) 313–315.
[5] H. Saito, Explosive Spalling of Prestressed Concrete in Fire, Building Research Insti-tute, Ministry of Construction, Japan, 1965.
[6] R. Jansson, Fire Spalling of Concrete: Theoretical and Experimental Studies, KTH Royal Institute of Technology, Stockholm, Sweden, 2013.
[7] X.-T. Chen, T. Rougelot, C.A. Davy, W. Chen, F. Agostini, F. Skoczylas, X. Bourbon, Experimental evidence of a moisture clog effect in cement-based materials under temperature, Cem. Concr. Res. 39 (2009) 1139–1148.
[8] R. Felicetti, F. Lo Monte, P. Pimienta, The influence of pore pressure on the fracture behaviour of concrete at high temperature, Cem. Concr. Res. (2014) (submitted for publication).
[9] R. Jansson, L. Boström, Factors influencing fire spalling of self compacting concrete, Mater. Struct. 46 (2013) 1683–1694.
[10] J. Tao, X. Liu, Y. Yuan, L. Taerwe, Transient strain of self-compacting concrete loaded in compression heated to 700 °C, Mater. Struct. 46 (2013) 191–201.
[11] P. Lura, O.M. Jensen, K. van Breugel, Autogenous shrinkage in high-performance cement paste: an evaluation of basic mechanisms, Cem. Concr. Res. 33 (2003) 223–232.
[12] O.M. Jensen, P.F. Hansen, Water-entrained cement-based materials II. Experimental observations, Cem. Concr. Res. 32 (2002) 973–978.

[13] P. Kalifa, G. Chene, C. Galle, High-temperature behaviour of HPC with polypropylene fibres: from spalling to microstructure, Cem. Concr. Res. 31 (2001) 1487–1499.
[14] D.P. Bentz, Fibers, percolation, and spalling of high-performance concrete, ACI Mater. J. 97 (2000) 351–359.
[15] C.E. Majorana, V.A. Salomoni, G. Mazzucco, G.A. Khoury, An approach for modelling concrete spalling in finite strains, Math. Comput. Simul. 80 (2010) 1694–1712.
[16] M. Ozawa, S. Uchida, T. Kamada, H. Morimoto, Study of mechanisms of explosive spalling in high-strength concrete at high temperatures using acoustic emission, Constr. Build. Mater. 37 (2012) 621–628.
[17] F. Ulm, P. Acker, M. Lévy, The "chunnel" fire. II: analysis of concrete damage, J. Eng. Mech. 125 (1999) 283–289.
[18] P. Lura, G.P. Terrasi, Reduction of fire spalling in high-performance concrete by means of superabsorbent polymers and polypropylene fibers: small scale fire tests of carbon fiber reinforced plastic-prestressed self-compacting concrete, Cem. Concr. Compos. 49 (2014) 36–42.
[19] G.H.A. van der Heijden, L. Pel, O.C.G. Adan, Fire spalling of concrete, as studied by NMR, Cem. Concr. Res. 42 (2012) 265–271.
[20] E.H. Lehmann, P. Vontobel, L. Wiezel, Properties of the radiography facility NEUTRA at SINQ and its potential for use as European reference facility, Nondestruct. Test. Eval. 16 (2001) 191–202.
[21] H. Justnes, K. Bryhn-Ingebrigtsen, G. Rosvold, Neutron radiography: an excellent method of measuring water penetration and moisture distribution in cementitious materials, Adv. Cem. Res. 6 (1994) 67–72.
[22] B. Weber, M. Wyrzykowski, M. Griffa, S. Carl, E. Lehmann, P. Lura, Neutron radiography of heated high-performance mortar, MATEC Web of Conferences, 6, 2013, p. 03004.
[23] M. Kanematsu, I. Maruyama, T. Noguchi, H. Iikura, N. Tsuchiya, Quantification of water penetration into concrete through cracks by neutron radiography, Nucl. Inst. Methods Phys. Res. A 605 (2009) 154–158.
[24] R. Jansson, L. Boström, The influence of pressure in the pore system on fire spalling of concrete, Fire. Technol 46 (2010) 217–230.
[25] M.R. Bangi, T. Horiguchi, Pore pressure development in hybrid fibre-reinforced high strength concrete at elevated temperatures, Cem. Concr. Res. 41 (2011) 1150–1156.
[26] L. Pel, S. Jaspers, F. Pereira, P. Pimienta, H. Carré, Combined NMR moisture, temper-ature and pressure measurements during heating, MATEC Web of Conferences, EDP Sciences, 2013, p. 03005.
[27] R. Felicetti, F. Lo Monte, P. Pimienta, The influence of pore pressure on the apparent tensile strength of concrete, 7th International Conference on Structures in Fire Zu-rich, Switzerland, 2012.
[28] M. Wyrzykowski, P. Lura, Controlling the coefficient of thermal expansion of cemen-titious materials — a new application for superabsorbent polymers, Cem. Concr. Compos. 35 (2013) 49–58.
[29] P. Trtik, B. Münch, W.J. Weiss, G. Herth, A. Kaestner, E. Lehmann, P. Lura, Neutron tomography investigation of water release from superabsorbent polymers in cement paste, International Conference on Material Science Aachen, Germany, 2010.
[30] M. Wyrzykowski, P. Lura, F. Pesavento, D. Gawin, Modeling of water migration dur-ing internal curing with superabsorbent polymers, J. Mater. Civ. Eng. 24 (2012) 1006–1016.
[31] J. Justs, M. Wyrzykowski, D. Bajare, P. Lura, Internal curing by superabsorbent poly-mers in ultra-high performance concrete, Cem. Concr. Compos. (2014) (in preparation).
[32] R. Hassanein, E. Lehmann, P. Vontobel, Methods of scattering corrections for quantitative neutron radiography, Nucl. Inst. Methods Phys. Res. A 542 (2005) 353–360.
[33] R.K. Hassanein, Correction methods for the quantitative evaluation of thermal neu-tron tomography, ETH Zurich, Zurich, 2006.
[34] M. Sedighi-Gilani, M. Griffa, D. Mannes, E. Lehmann, J. Carmeliet, D. Derome, Visual-ization and quantification of liquid water transport in softwood by means of neu-tron radiography, Int. J. Heat Mass Transf. 55 (2012) 6211–6221.
[35] X. Liu, G. Ye, G. De Schutter, Y. Yuan, L. Taerwe, On the mechanism of polypropylene fibres in preventing fire spalling in self-compacting and high-performance cement paste, Cem. Concr. Res. 38 (2008) 487–499.
[36] A. Witek, D. Gawin, Experimental and numerical study on the efficiency of the poly-propylene fibers admixture in reducing pore pressure in heated concrete, J. Build. Phys. 38 (2014) 121–137.